ORNL/CP-96312

CONF-980708--

Evaluation of Constraint Methodologies Applied to a Shallow-Flaw Cruciform Bend Specimen Tested under Biaxial Loading Conditions*

B. R. Bass, W. J. McAfee, P. T. Williams, and W. E. Pennell

Oak Ridge National Laboratory
P. O. Box 2009
Oak Ridge, TN, 37831-8056

Submitted for presentation at the
1998 ASME/JSME JOINT
PRESSURE VESSELS AND PIPING CONFERENCE
SAN DIEGO, CALIFORNIA
JULY 26-30, 1998

Abstract

A technology* to determine shallow-flaw fracture toughness of reactor pressure vessel (RPV) steels is being developed for application to the safety assessment of RPVs containing postulated shallow surface flaws. Matrices of cruciform beam tests were developed to investigate and quantify the effects of temperature, biaxial loading, and specimen size on fracture initiation toughness of two-dimensional (constant depth), shallow, surface flaws. The cruciform beam specimens were developed at Oak Ridge National Laboratory (ORNL) to introduce a prototypic, far-field, out-of-plane biaxial stress component in the test section that approximates the nonlinear stresses resulting from pressurized-thermal-shock or pressure-temperature loading of an RPV. Tests were conducted under biaxial load ratios ranging from uniaxial to equibiaxial. These tests demonstrated that biaxial loading can have a pronounced effect on shallow-flaw fracture toughness in the lower transition temperature region for RPV materials. The cruciform fracture toughness data were used to evaluate fracture methodologies for predicting the observed effects of biaxial loading on shallow-flaw fracture toughness. Initial emphasis was placed on assessment of stress-based methodologies, namely, the *J-Q* formulation, the Dodds-Anderson toughness scaling model, and the Weibull approach. Applications of these methodologies based on the hydrostatic stress fracture criterion indicated an effect of loading-biaxiality on fracture toughness; the conventional maximum principal stress criterion indicated no effect.

* Research Sponsored by the Office of Nuclear Regulatory Research, U.S. Nuclear Regulatory Commission under Interagency Agreement 1886-8663-1W with the U.S. Department of Energy under Contract DE-AC05-96OR22464 with Lockheed Martin Energy Research Corp.

1. Introduction

The Heavy-Section Steel Technology (HSST) Program at Oak Ridge National Laboratory (ORNL) is developing technology to determine the shallow-flaw fracture toughness of steels for application to the safety assessment of reactor pressure vessels (RPVs). In the lower transition temperature region, shallow-flaw fracture toughness data for RPV materials exhibit mean values and scatter that are greater than those for deep flaws because of the relaxation of crack-tip constraint [1]. Previously, uniaxial full-thickness clad beam tests [2] were used to quantify this shallow-flaw effect in specimens (taken from an RPV of a canceled nuclear plant) which are prototypic of RPV wall thickness and material properties. However, the uniaxial beam tests did not address the issue of near-surface biaxial stress fields produced by pressurized-thermal-shock (PTS) or pressure-temperature (P-T) loading of an RPV (see Fig. 1). The out-of-plane biaxial stress component has the potential to increase constraint at the tip of a shallow crack and thereby reduce the shallow-flaw fracture toughness enhancement.

Cruciform beam specimens [3-7] developed at ORNL introduce a prototypic, far-field, out-of-plane biaxial stress component in the test section that approximates the nonlinear stresses of PTS or P-T loading (see Fig. 2). The cruciform specimen permits controlled application of biaxial loading ratios resulting in controlled variations of crack-tip constraint for shallow surface flaws. The biaxial load ratio is defined as P_T / P_L, where P_T is the total load applied to the transverse beam arms and P_L is the total load applied to the longitudinal arms. A special test fixture was also designed and fabricated permitting testing under uniaxial loading, P_T / P_L ratio of (0:1), and two biaxial loading ratios, P_T / P_L ratios of (0.6:1) and (1:1). The specimen and test fixture have been described extensively in prior HSST publications [3-5].

Matrices of cruciform beam tests were defined within the HSST Program to evaluate biaxial loading effects on the fracture toughness of 2-dimensional (2-D) (infinite-length) [3] and 3-D (finite-length)

DISCLAIMER

[7] shallow surface flaws. An A 533 B steel, heat treated to obtain an elevated yield strength, was fabricated into cruciform specimens incorporating 2-D flaws and tested with the load ratio and temperature as independent parameters [3]. Fracture toughness tests were run with biaxial load ratios, P_T / P_L, of (0:1), (0.6:1), and (1:1). Five different temperatures through the transition temperature region for toughness were sampled in this series. These test data are essential for validation of a cleavage fracture methodology that can predict the observed effects of biaxial loading on shallow-flaw toughness of RPV steels in the lower transition temperature region.

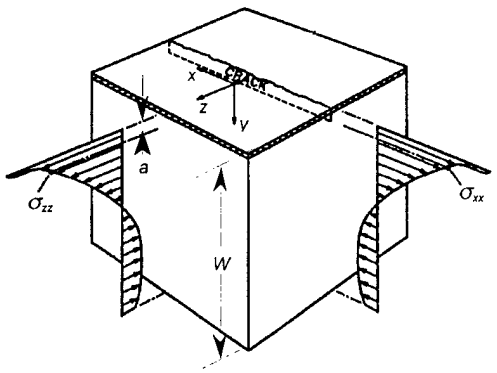

Fig. 1. PTS loading produces biaxial stress in an RPV wall with one of the principal stresses aligned parallel with the tip of the constant-depth shallow surface flaw.

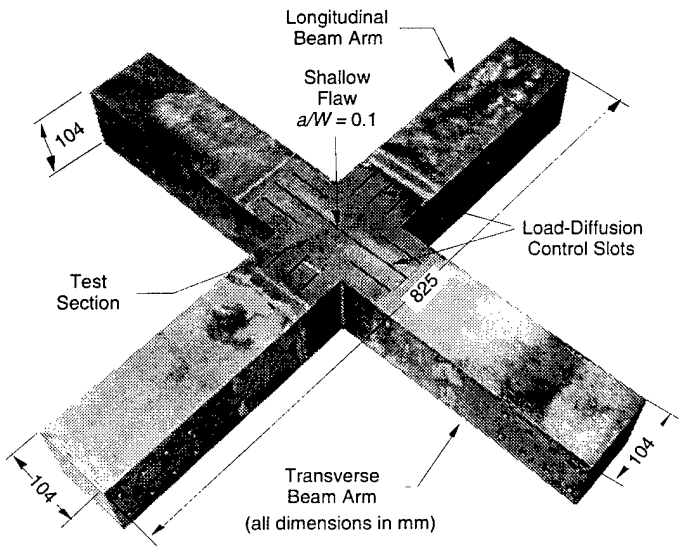

Fig. 2. Geometry of the cruciform shallow-flaw biaxial fracture toughness test specimen.

Conventional fracture-prevention technology has relied on the use of fracture correlation parameters (K or J) to characterize both the applied loading and the resistance of engineering materials to crack initiation. As documented in numerous references (for example, see ref. 8), the shortcomings of these one-parameter cleavage-fracture methodologies have been addressed using different strategies that share a common emphasis on in-plane maximum principal (opening-mode) stress as the relevant criterion for unstable crack propagation. O'Dowd and Shih [9] introduced a correlative approach based on the two-parameter J-Q description of the crack-tip fields. In that model, the Q-stress parameter characterizes the level of near-tip stress triaxiality (relative to small-scale yielding conditions) over distances extending a few crack-tip-opening displacements (CTODs) ahead of the crack tip. Dodds and Anderson (D-A) [10-11] employed a local fracture criterion in their toughness scaling model to characterize the relative effects of constraint on cleavage toughness. In the D-A model, the local fracture criterion is based on the material volume ahead of the crack front over which the maximum principal stress exceeds a critical value. Other stress-based local approaches adopted the Weibull stress [12] as a fracture parameter that reflects local damage near the crack tip and reaches a critical value at material failure. Conventional applications of the Weibull methodology utilize the maximum principal stress as the equivalent tensile stress in the integral representation of the Weibull stress.

Initial emphasis in the HSST studies was placed on assessment of three stress-based methodologies (J-Q formulation, D-A scaling model, and Weibull approach) as applied to the cruciform specimen and biaxial fracture toughness data. McAfee et al. [5] demonstrated that the J-Q methodology and D-A toughness scaling model predicted essentially no effect of biaxial loading on cleavage fracture toughness in the cruciform bend specimen when the maximum principal stress is adopted as the fracture criterion. The latter result provided motivation for considering alternative fracture criteria that are sensitive to multiaxial loading states.

A number of previous studies (for example, see refs. 13-15) investigated alternative fracture criteria using extended weakest-link models suitable for brittle materials (e.g., ceramics) subjected to multiaxial loading. These models consider flaws as planar cracks, with the loading expressed in terms of some suitably defined equivalent stress which depends on the orientation of the crack plane in the local stress field. Selected equivalent stress functions defined in terms of multiaxial stress components were used to evaluate failure criteria through applications to measured data. Another alternative is the hydrostatic stress function, which has been applied as a critical fracture parameter. Weiss [16] described an experimental program in which he investigated the effects of stress biaxiality on fracture strain and successfully reconciled measured data using a critical hydrostatic stress fracture criterion. Also, the J-Q methodology utilized an operational definition of the Q-stress expressed in terms of the hydrostatic stress [17], which is consistent with its interpretation as a triaxiality parameter.

Recently, analyses of the cruciform specimen were performed within the HSST Program using the hydrostatic stress as the failure criterion in the stress-based methodologies, in place of the maximum principal stress. This paper provides an interim report on the results of these analyses. The following sections present a summary of the HSST biaxial testing program, the test results and fracture toughness determinations, and finally applications of the constraint methodologies to the cruciform specimen and measured data from the biaxial testing program.

2. Specimen Configuration and Testing Facility

The cruciform beam specimens are fabricated with a test section that has dimensions of 104 mm × 104 mm × 104 mm (see Fig. 2). A 2-D shallow flaw of depth a = 10 mm (a/W = 0.1) is fabricated into the specimen. Load-diffusion control slots are machined into the specimen loading arms to create the boundary conditions required to achieve a uniform stress field in the central test section. For each cruciform specimen, fatigue-sharpening of the shallow 2-D flaw is completed before the transverse loading arms are attached by electron-beam (EB) welding. Measured temperature data taken during EB welding of the transverse arms imply that temperatures produced in the cruciform test section (< 150°C) are not high enough to initiate processes which would reduce fracture toughness, such as locally-intensified strain-aging embrittlement. The specimen design, coupled with a statically determinate load-reaction system, permits the specimen to be loaded in either uniaxial (4-point bending) or biaxial (8-point bending) configurations. Tests of nominally identical specimens can be performed with the level of stress biaxiality as the only loading test variable.

Instrumentation applied to the test specimens included thermocouples, strain gages, clip gages, and displacement transducers. Both crack-mouth-opening displacement (CMOD) and load-line displacement (LLD) were monitored continuously throughout each of the tests. Control of the test temperature was achieved with various liquid nitrogen distribution systems. Mechanical loading is applied to the cruciform specimens using a large-scale cruciform test fixture mounted in a 3.1 MN Instron servo-hydraulic testing machine at ORNL.

3. Material Preparation and Characterization

HSST Plate 14 (A 533 B steel) was the source material for the cruciform bend specimens. This plate was selected primarily because of its high carbon content which made it more responsive to increasing the yield strength by heat treatment. The base material underwent heat treatment to achieve an elevated yield strength approximating that of a typical radiation-sensitive RPV steel irradiated to a fluence of 1.5×10^{19} n/cm^2 (> 1 MeV). The heat treatment was performed successfully, providing a room temperature yield stress in the desired range. Fabrication of the cruciform specimens has been described in refs. 3, 5, and 6.

Characterization of the heat-treated material was performed to provide verification of properties and data for the determination of appropriate test conditions. Tensile, Charpy, drop-weight, and 1/2T compact tension specimens were tested. From Charpy V-notch (CVN) testing, T_{CV} was determined to be 56 °C (132 °F), and the drop-weight nil-ductility temperature (*NDT*) was found to be 40 °C (104 °F). Thus, *NDT* controlled the reference temperature, and RT_{NDT} = 40 °C. A comparison was made between the Charpy results for Plate 14 and data from the HSSI Fifth Irradiation Series Weld 73W [18] in the irradiated [1.51×10^{19} n/cm^2 (> 1 MeV)] condition (see Fig. 3). From this comparison, it was observed that the trend of the Charpy data for Plate 14 very nearly matched that of the irradiated 73W [18]. It can be concluded that the heat treatment was successful in providing the desired material properties.

American Society for Testing and Materials (ASTM) standard 6.35-mm (0.25-in.) gage diameter tensile specimens were machined from material near the midplane of the plate and at four locations through the half thickness. To characterize temperature dependency, tests were performed at four different temperatures using specimens taken from a single layer near the mid-plane of the plate. These test temperatures — -30 °C (-22 °F), 10 °C (50 °F), 40 °C (104 °F), and 60 °C (140 °F) — were selected as representative of the anticipated test temperature range for the cruciform specimens in the verification test matrix. Four locations through the thickness of the plate were also sampled. The variation of tensile properties with both temperature and location through the plate thickness was observed to be relatively small. Temperature-dependent material properties representing stress-strain behavior for this material at -30 °C and -5 °C are given in Table 1.

A series of 1/2T compact specimens, taken from different locations within the parent plate, were tested over the range of -130 °C to room temperature. This data set was used to determine a reference temperature T_0 based on the *Master Curve* approach [19]. First, the 1/2T data were adjusted to a 1T constraint condition using

$$K_{1T} = 20 + \left(K_{1/2T} - 20\right)\left(0.5/1\right)^{\frac{1}{4}} . \quad (1)$$

The valid data were then fitted using the Master Curve equation,

$$K_{J_c}(\text{med}) = 30 + 70\exp\left[0.019\left(T - T_0\right)\right] , \left[\text{MPa}\sqrt{\text{m}}\right] , \quad (2)$$

from which a value of T_0 = -37.3 °C (-35.1 °F) was determined. Thus, there was a difference of 77.3 °C (139.1 °F) between the RT_{NDT} and T_0 normalizing temperatures.

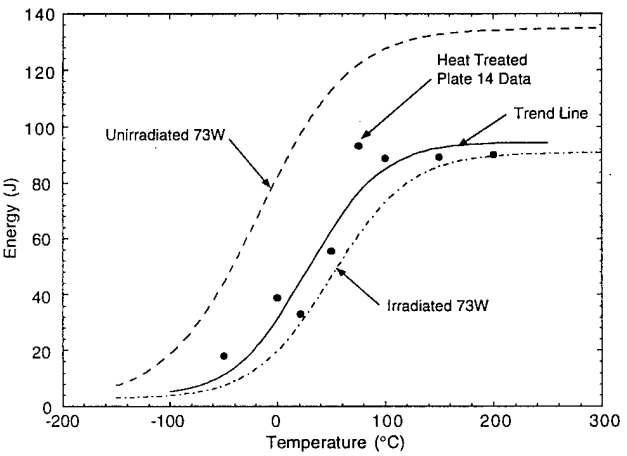

Fig. 3. Comparison of Charpy curves from heat-treated Plate 14 material with that from irradiated 73W material.

4. Testing of Cruciform Specimens

Six cruciform specimens were tested at -30 °C (T - T_0 = 7 °C) to provide data for (a) three biaxial load ratios and (b) two duplicate tests at each condition. The load v. CMOD data for these specimens are shown in Fig. 4, which compares the centerline CMOD for each of these six specimens. The deformation response for all specimens was in good agreement. The specimens exhibited very little plastic

deformation as measured by both CMOD and LLD, regardless of the applied biaxial load. Variation of failure conditions, load and deformation (CMOD and LLD), seemed to vary randomly; i.e., there was no clear correlation between applied biaxial loading and failure load or deformation. Examination of the fracture surfaces showed that initiation occurred within the center 50 mm of flaw front, indicating that the cleavage initiation toughness values were not influenced by edge conditions.

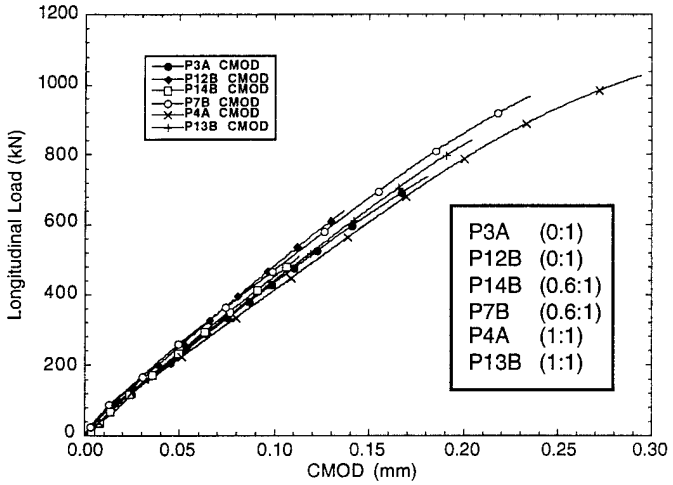

Fig. 4. Comparison of CMOD responses for cruciform specimens tested at -30 °C (-22 °F) for load ratios of (0:1), (0.6:1), and (1:1).

The estimated toughness values for these specimens are shown in Table 2. Estimates were made using CMOD and LLD results, the measured crack depth at the probable initiation site, and the η-factor procedures that have been used previously in estimating toughness from shallow-flaw tests [1, 6]. The values for all these tests are near the estimated lower shelf toughness for this material, which is consistent with the observed deformation behavior, i.e., elastic tests. For cases where primarily elastic deformation occurs, biaxial loading would be expected to have little effect on constraint at the flaw tip, and thus little effect on toughness. The elastic response of these specimens gave an indication that the test temperature might be too low (i.e., -30 °C was on or nearly on the lower shelf) to produce a biaxial loading effect.

A second set of nine cruciform specimens was tested at a nominal test temperature of -5 °C (23 °F) (normalized temperature $T - T_0$ = 32 °C). This higher temperature was expected to provide a better balance between cleavage behavior and accumulated plasticity at failure for evaluation of biaxial effects on toughness. Three specimens each were tested under uniaxial (0:1), biaxial (0.6:1), and equibiaxial (1:1) loadings as shown in Table 2. Deformation responses of longitudinal load v. CMOD results are shown in Fig. 5. The longitudinal load v. CMOD traces for these specimens were comparable, but the failure deformation magnitudes and scatter exhibited a strong dependence on the applied biaxial load as shown in Fig. 5. The unload/reload deformation trace of Specimen P2B was due to initial interference with the transverse beam arm load seats. The test was interrupted; the specimen was unloaded; and the fixture was then reconfigured while holding the specimen temperature near -5 °C. It was concluded from post-test evaluation that this perturbation in the load histogram was insignificant as far as affecting the final toughness results.

Additional tests were performed at higher temperatures to investigate fracture behavior through the lower/mid-transition curve. The uniaxial tests at -5 °C indicated borderline plastic collapse; therefore, no additional uniaxial specimens were tested at higher temperatures. Biaxial (0.6:1) and (1:1) tests were performed near 5 °C and 15 °C, as shown in Table 2. Although scatter in the data set increased, the clear distinction between the effect on toughness of different biaxial load ratios was retained.

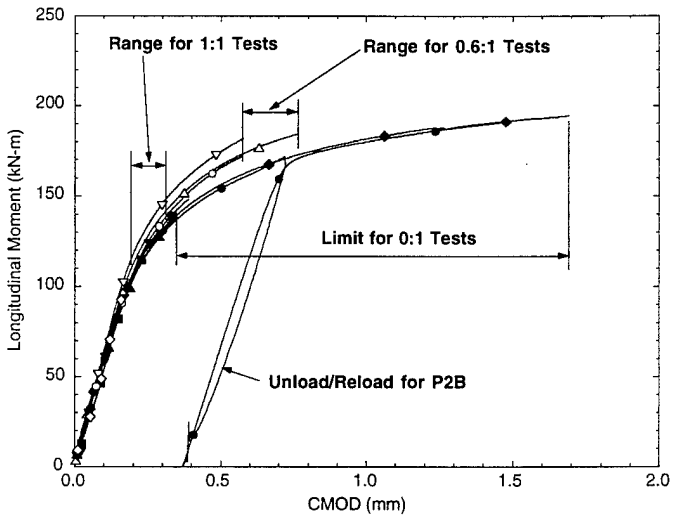

Fig. 5. Comparison of CMOD responses for cruciform specimens at nominal test temperature of -5 °C (23 °F) for load ratios of (0:1), (0.6:1), and (1:1).

5. Fracture Toughness Determination

Three-dimensional elastic-plastic finite element analyses of the cruciform specimen were performed with the ABAQUS program [20] to generate η-factors for determination of fracture-toughness values from test data. For the -30 °C tests, generally good agreement was obtained for the deformation response, as expected since the tests were essentially elastic. These analyses over-predicted the stiffness of the specimen, with this over-prediction being greatest for the biaxial (1:1) load case. A comparison of analysis and experiment is shown in Fig. 6 for this biaxial case. For the tests performed at -5 °C, the agreement was dependent on the biaxial load ratio. Good agreement was obtained between the biaxial (1:1) analytical and experimental results; however, comparison of the uniaxial results showed the analysis to predict substantially stiffer longitudinal load v. CMOD responses than were measured in the test (see Fig. 7).

These test results demonstrated a significant effect of biaxial loading on shallow-flaw fracture toughness. The estimated toughness values are shown graphically in Figs. 8 and 9 for the -30 °C and -5 °C test sets, respectively. The -30 °C specimens behaved in an elastic manner and little biaxial effect was observed. For the six

Table 1. Properties Used in Finite-Element Analyses of Heat-Treated Plate 14 Cruciform Specimens

Property	Temperature	
	-30 °C (-22 °F)	-5 °C (23 °F)
Young's Modulus [MPa (ksi)]	182,720 (26,500)	182,720 (26,500)
Poisson's Ratio	0.25	0.25
Proportional Limit [MPa (ksi)]	534 (77.5)	512 (74.2)
Ultimate Strength [MPa (ksi)]	848 (123)	828 (120.2)

Table 2. Summary of Heat-Treated Plate 14 Cruciform Specimen Test Results

Spec.	Test Temp. [°C (°F)]	Biaxiality Ratio	Failure Load [kN (kips)]	Failure LLD [mm (in.)]	Failure CMOD [mm (in.)]	η-Factor P-LLD	K_J from P-LLD [MPa√m (ksi√in)]	η-Factor P-CMOD	K_J from P-CMOD [MPa√m (ksi√in)]
P2A[1]	38 (100)	0:1	1785.2 (401.3)	29.561 (1.1638)	2.0269 (.0798)	NA	NA	NA	NA
P12B	-30 (-22)	0:1	638.4 (143.5)	1.938 (.0763)	.1372 (.0054)	4.197	76.3 (69.5)	5.705	88.0 (80.1)
P3A	-31 (-24)	0:1	736.1 (165.5)	2.276 (.0896)	.1753 (.0069)	3.011	97.2 (88.4)	4.911	103.0 (93.7)
P14B	-31 (-24)	0.6:1	508.2 (114.3)	1.504 (.0592)	.1118 (.0044)	6.877	99.6 (90.7)	6.217	70.3 (64.0)
P7B	-30 (-22)	0.6:1	965.8 (217.1)	2.802 (.1103)	.2362 (.0093)	1.379	129.2 (117.6)	3.612	136.3 (124.0)
P13B	-28 (-18)	1:1	840.4 (188.9)	2.398 (.0944)	.2032 (.0080)	2.693	97.9 (89.1)	4.547	112.1 (102.0)
P4A	-29 (-21)	1:1	1026.7 (230.8)	2.936 (.1156)	.2946 (.0116)	.892	139.7 (127.1)	3.265	141.2 (128.5)
P2B.1	-4 (24)	0:1	1351.0 (303.7)	7.330 (.2886)	.7036 (.0277)	.436	245.3 (223.2)	3.428	261.5 (238.0)
P2B.2	-3 (26)	0:1	1504.4 (338.2)	13.774 (.5423)	1.4173 (.0558)	.343	346.2 (315.1)	3.177	375.5 (341.8)
P9A	-3 (26)	0:1	1529.0 (343.7)	14.575 (.5738)	1.6916 (.0666)	.327	354.3 (322.5)	3.149	394.5 (359.1)
P3B	-4 (24)	0.6:1	1449.6 (325.9)	8.440 (.3323)	.7645 (.0301)	.323	266.1 (242.2)	3.223	266.8 (242.8)
P12A	-6 (21)	0.6:1	1349.4 (303.4)	5.923 (.2332)	.5715 (.0225)	.388	212.5 (193.4)	3.166	223.6 (203.5)
P6B	-4 (24)	1:1	1096.0 (246.4)	3.637 (.1432)	.3505 (.0138)	.685	166.9 (151.9)	3.126	162.3 (147.8)
P15A	-4 (25)	1:1	1072.6 (241.1)	3.424 (.1348)	.3150 (.0124)	.716	155.9 (141.6)	3.175	153.9 (140.1)
P4B	6 (42)	1:1	1118.5 (251.5)	4.651 (.1831)	.3353 (.0132)	.686	183.2 (166.7)	3.430	167.5 (152.5)
P6A	4 (40)	0.6:1	1255.1[2] (282.2)	5.210 (.2051)	.4089 (.0161)	.444	204.3 (186.0)	3.384	195.2 (177.6)
P10A	8(46)	0.6:1	1570.8 (353.2)	10.714 (.4218)	0.9042 (.0356)	0.309	308.1 (280.4)	3.376	298.3 (271.5)
P7A	15 (60)	1:1	1303.7[2] (293.1)	6.012 (.2367)	.6121 (.0241)	.611	248.3 (226.0)	3.444	229.3 (208.7)
P11A	16 (60)	1:1	1419.5[2] (319.1)	6.932 (.2729)	.5563 (.0219)	.372	246.9 (224.7)	3.351	234.1 (213.1)
P9B	16 (60)	0.6:1	1500.9[2] (337.4)	9.766 (.3845)	.8204 (.0323)	.334	294.7 (268.2)	3.397	281.9 (256.5)
P11B	17 (62)	1:1	1456.5[2] (327.5)	9.934 (.3911)	1.0897 (.0429)	.584	352.8 (321.0)	3.585	325.5 (296.2)
P10B	-6 (22)	1:1	1246.2[2] (280.2)	5.260 (.2071)	.4801 (.0189)	.616	230.2 (209.5)	3.377	204.6 (186.2)
P15B	-4 (25)	0.6:1	1431.1[2] (321.7)	7.537 (.2967)	.5791 (.0228)	.332	248.1 (225.8)	3.227	232.4 (211.5)
P13A	-6 (21)	0:1	1165.1[2] (261.9)	5.250 (.2067)	.3912 (.0154)	.785	217.3 (197.8)	4.831	184.2 (167.6)

[1]Test discontinued, no cleavage.
[2]Failure load based on equivalent 254 mm (10 in.) beam arm length.

specimens tested, the toughness increased slightly with an increase in biaxial ratio. It is expected that additional specimens would show statistically no difference between uniaxial and biaxial loading at this temperature. For the tests performed at -5 °C, the effect of biaxiality was pronounced, as is shown in Fig. 9. The mean value of the biaxial (1:1) loading resulted in approximately a 42 percent decrease from the mean uniaxial toughness ($K_{Jc\,(1:1)} / K_{Jc\,(0:1)} = 0.58$). One feature of these tests also apparent in Figs. 8 and 9 is the reduced scatter for specimens tested under biaxial loading at comparable loads and temperatures.

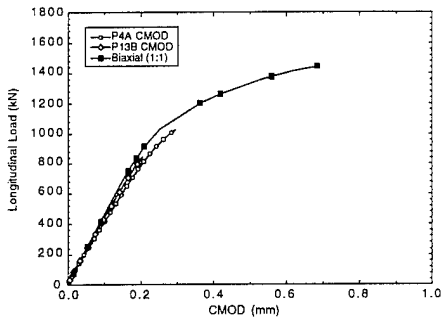

Fig. 6. Comparison of predicted and measured CMOD for biaxially (1:1) loaded cruciform test at -30 °C (-22 °F).

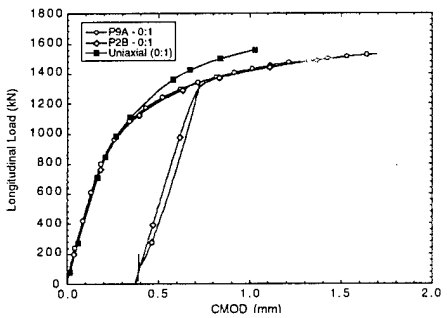

Fig. 7. Comparison of predicted and measured CMOD for uniaxially (0:1) loaded cruciform test at -5°C (23°F).

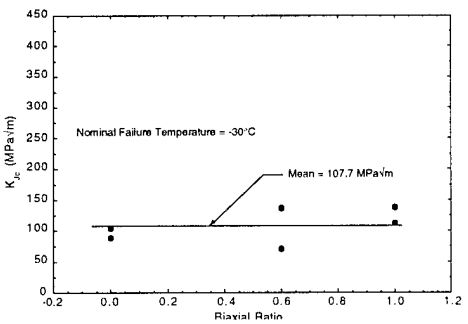

Fig. 8. Data determined for heat-treated Plate 14 tested at -30° C (-22 °F) indicating no effect of biaxial load ratio on fracture toughness at the lower-shelf temperature.

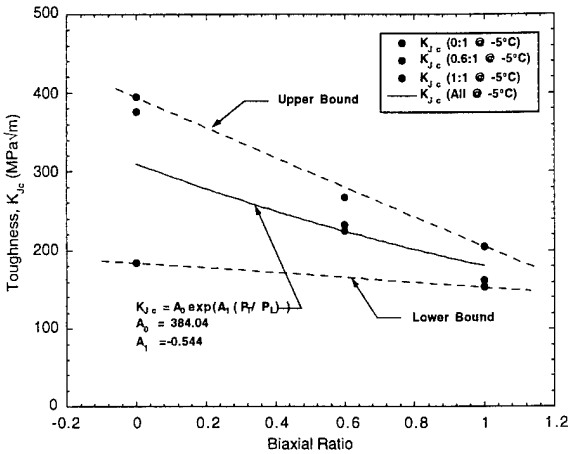

Fig. 9. The effect of biaxial load ratio on fracture toughness determined for heat-treated Plate 14 tested at -5 °C (23 °F).

Figure 10 is a summary of all the cruciform data generated in this test series presented as a function of normalized test temperature ($T - T_0$). Trend curves were developed through these data to provide a visual interpretation of the relationship between biaxial loading and temperature. Note that these trend curves are not rigorous fits to all the data but are intended primarily to identify and separate data sets. The curves were all normalized to the same toughness values for normalized temperatures less than 0 °C. These toughness values were developed using data from the 1/2T CT specimens tested on the lower shelf which were then adjusted to a full-constraint condition using the modified Irwin β_{Ic} approach [21]. Also, the mean of the data set for the cruciform tests at -30 °C was used as a common point for all three curves. The trend curve for the (0.6:1) data was developed by ratioing the biaxial (1:1) trend line upward so that it would pass through the centroid of the (0.6:1) data set. Figure 10 shows the development of a family of curves, each corresponding to a particular biaxial load ratio. The biaxial (1:1) data form a lower bound to this data set. Based on these trend lines, the *mean* of the estimated toughness values from the uniaxial tests increases much more sharply with increasing temperature than do those of the biaxial tests.

6. Applications of Constraint Methodologies

6.1 Analysis of Local Crack-Tip Fields

Three-dimensional finite-element models were developed for local crack-tip field analyses of the cruciform bend specimen subjected to the uniaxial and biaxial loading conditions represented by the test data in Fig. 9. The finite-element model shown in Fig. 11a consists of 20,754 nodes and 4317 20-node isoparametric brick elements. The initial finite-root-radius at the crack tip was 0.0254 mm (0.001 in.) (see Fig. 11b). Corresponding *J*-integrals were calculated with a separate sharp-crack model (not shown) to obtain a more accurate determination of *J* as a function of loading. Both models were analyzed with the ABAQUS code utilizing a nonlinear elastic-plastic constitutive formulation with incremental loading of the specimen. Temperature-dependent properties were

taken from tensile characterization tests of the heat-treated Plate 14 material (see Table 1 and ref. 3). All model results reported herein assumed a specimen temperature of -5 °C, consistent with the toughness data shown in Fig. 9. Also, these assessments neglected the potential impact of ductile tearing observed in two of the uniaxially loaded cruciform specimens, tested at -5 °C and failed at high toughness values (see Fig. 9).

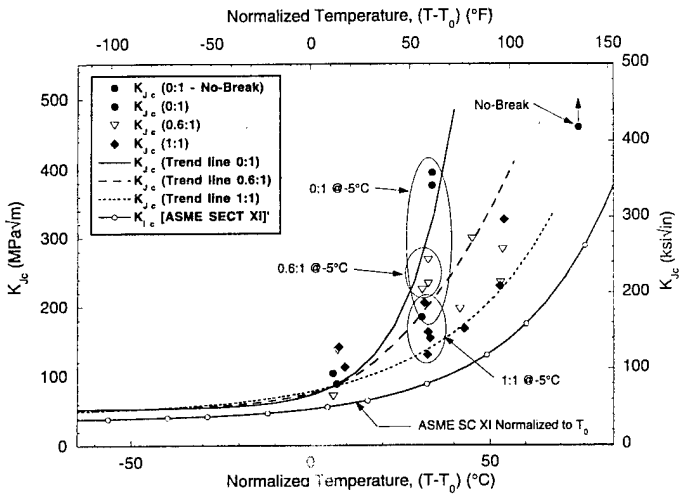

Fig. 10. A summary of all heat-treated Plate 14 cruciform data presented as a function of normalized (T-T_0) test temperature. Trend curves fitted to data provide a visual interpretation of relationship between biaxial loading and temperature.

Results generated from these local crack-tip field analyses include the profiles of effective stress, σ_{eff}, and total effective plastic strain, ε_p, depicted in Fig. 12 for the uniaxial (0:1) and biaxial (x:1) (x = 0.6 and 1.0) loading cases. The parameters are computed at $J \approx 131$ kJ/m^2 (0.75 in.-kip/in^2), which corresponds approximately to a measured fracture toughness data point for biaxial (1:1) loading depicted in Fig. 9. Profiles of these parameters are plotted versus distance r in front of the crack tip (θ=0, Fig. 11b) normalized by J/σ_0, where σ_0 is the proportional limit of 512 MPa (74.2 ksi). These fields clearly demonstrate that biaxial loading suppresses development of plasticity in front of the crack tip, with the effect becoming more pronounced with increasing biaxiality ratio.

6.2 J-Q Theory

O'Dowd and Shih [9] developed the J-Q methodology in which the J-integral sets the scale of deformation at the crack tip, and the hydrostatic stress parameter, Q, quantifies the level of stress triaxiality over distances of approximately $1 < r/(J/\sigma_0) < 5$ ahead of the crack tip. The annular zone over which the family of stress fields described by

$$\frac{\sigma_{ij}}{\sigma_0} = f_{ij}\left(\frac{r}{J/\sigma_0}, \theta\ ;\ Q\right) \qquad (3)$$

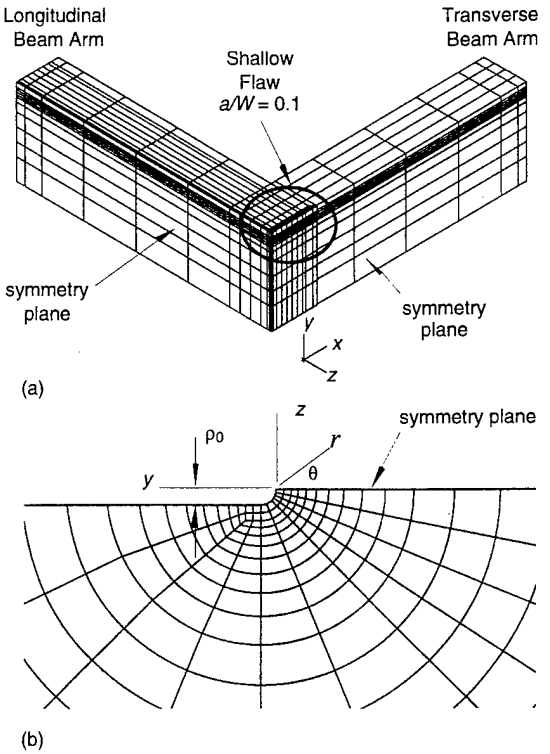

Fig. 11. Mesh layout for cruciform finite-element model: (a) the complete model and (b) a closeup of the finite-root-radius crack tip: 20,754 nodes, 4317 elements (20-node quadratic), root-tip radius ρ_0 = 0.0254 mm (0.001 in.).

accurately determines the actual field is called the *J-Q annulus*. In Eq. (3), r and θ are cylindrical coordinates (Fig. 11b) with the origin at the crack tip. The crack-tip stress fields within the J-Q annulus were represented by the sum of a J-dominant reference solution and a difference field $(\sigma_{ij})_{DIFF}$. O'Dowd and Shih [9] observed that the difference field corresponds approximately to a uniform hydrostatic shift in the stress field in front of the crack tip. They designated the amplitude of this approximate difference field by the letter Q,

$$\sigma_{ij} \approx (\sigma_{ij})_{Q=0} + Q\,\sigma_0\delta_{ij} \quad (|\theta| \le \pi/2)\ . \qquad (4)$$

Two operational definitions of the Q-family of fields are presented in ref. 17. The first definition is given in terms of the opening-mode stress, σ_{zz},

$$Q = \frac{\sigma_{zz} - (\sigma_{zz})_{SSY;Q=0}}{\sigma_0} \text{ at } \theta = 0,\ \frac{r}{(J/\sigma_0)} = 2\ , \qquad (5)$$

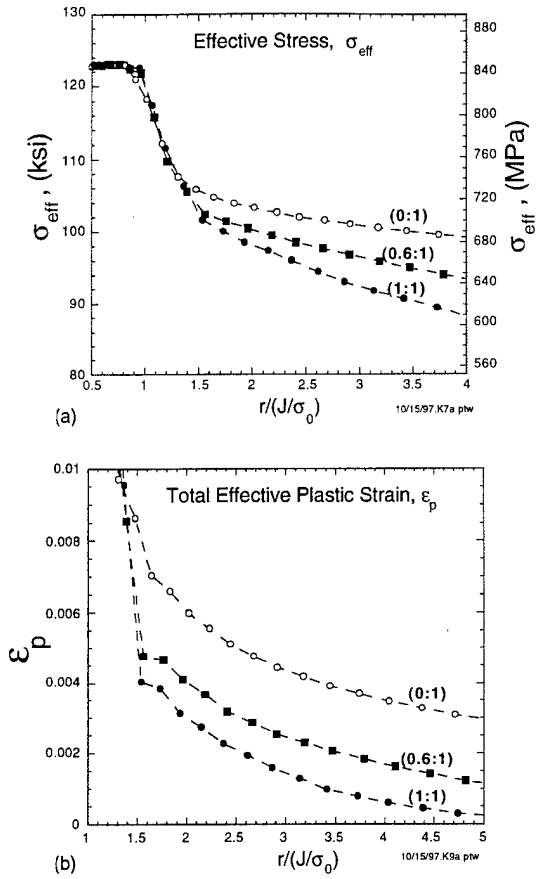

Fig. 12. Profiles of (a) effective stress, σ_{eff}, and (b) total effective plastic strain, ε_p, for uniaxial (0:1) and biaxial (x:1) loading cases at $J \approx 131$ kJ/m^2 (0.75 in.-kip/in^2).

where SSY refers to the *small-scale-yielding* reference solution. The second definition, which is consistent with the interpretation of Q as a triaxiality parameter, is based on the hydrostatic stress, σ_H,

$$Q_H = \frac{\sigma_H - (\sigma_H)_{SSY;Q=0}}{\sigma_0} \text{ at } \theta = 0,\ \frac{r}{(J/\sigma_0)} = 2 \quad . \qquad (6)$$

where σ_H (also known as the *mean stress*) is $\frac{1}{3}$ of the first invariant of the Cauchy stress tensor. These two operational definitions of Q-stress are applied in Fig. 13 to the local crack-tip field analysis of the uniaxially-loaded cruciform bend specimen. Normalized opening-mode stress versus normalized distance in front of the crack tip is compared with SSY results for a range of J-values in Fig. 13a; results based on the hydrostatic stress are shown in Fig. 13b. The SSY solution was developed using a 2-D plane strain model with the same finite-root-tip geometry and material properties as the 3-D finite strain model. For the uniaxially-loaded specimen, the two definitions of Q-stress provide results that are equivalent, a result confirmed previously in ref. 17.

In Fig. 14, opening-mode stress profiles for the three loading cases under study are plotted with the SSY solution. In Fig. 14a, the Q-stresses calculated using the first definition for Q, Eq. (5), do not present significant differences among the loading cases due to the observed insensitivity of the opening-mode stress to biaxial loading. The second definition, Eq. (6), was used in Fig. 14b to calculate a Q_H-stress based on the hydrostatic stress profiles. At a nominal J-level of 131 kJ/m^2, the Q_H-stress differentiates between the different levels of biaxiality, such that the Q_H-stress decreases (in absolute value) monotonically with increasing biaxiality ratio. The peak values of normalized stress coincide for the three loading cases. In contrast to the uniaxial loading case, the difference fields for the biaxial loading cases vary with normalized distance over the range of $1 < r/(J/\sigma_0) < 5$; i.e., they do not correspond to a uniform shift in the hydrostatic stress field relative to the 2-D SSY solution.

In Fig. 15, the two definitions of Q-stress are plotted as a function of normalized J to determine their evolution over the loading path for the three biaxiality loading ratios. These curves terminate approximately at J-values corresponding to fracture toughness data points given in Fig. 9 for the three loading conditions. The J-integral in Fig. 15 has been normalized by the initial crack depth, a, and the proportional limit, σ_0. For both definitions of Q, the loss-of-constraint increases with increasing load. The Q-stress based on the opening mode stress (Fig. 15a) shows no significant differentiation among the three loading cases. For the biaxial (0.6:1) and equibiaxial (1:1) loading cases, the Q_H parameter based on the hydrostatic stress (Fig. 15b) diverges from the uniaxial (0:1) path as the load level increases. A conventional interpretation of the Q_H parameter in Fig. 15b is that a higher level of crack-tip constraint is maintained under increasing load as the biaxiality ratio is varied from uniaxial (0:1) to equibiaxial (1:1) conditions.

6.3 Cleavage Toughness Scaling Model

Dodds and Anderson (D-A) [10-11] quantified effects of constraint on cleavage fracture toughness using a toughness scaling model that couples the global parameter J with a local failure criterion. The D-A model adopts the material volume ahead of the crack tip, over which the normalized maximum principal stress (σ_3 / σ_0) exceeds a critical value, as the local fracture criterion. The convention applied in this paper for ordering the principal stresses is $\sigma_3 \geq \sigma_2 \geq \sigma_1$, where σ_3 is essentially equivalent to the opening-mode stress, σ_{zz}, in the cruciform specimen. The toughness scaling model requires that equal stressed volumes (or equal areas in 2-D models) be attained ahead of the crack tip for cleavage fracture to be realized in different specimens. Equality of stressed volumes implies an equal probability of achieving cleavage fracture, even though J-values may be markedly different.

For the plane strain model described in ref. 17, the normalized maximum principal stress has the approximate form

$$\frac{\sigma_3}{\sigma_0} = f_0\left(\frac{r}{(J/\sigma_0)}, \theta\right) + Q \quad . \qquad (7)$$

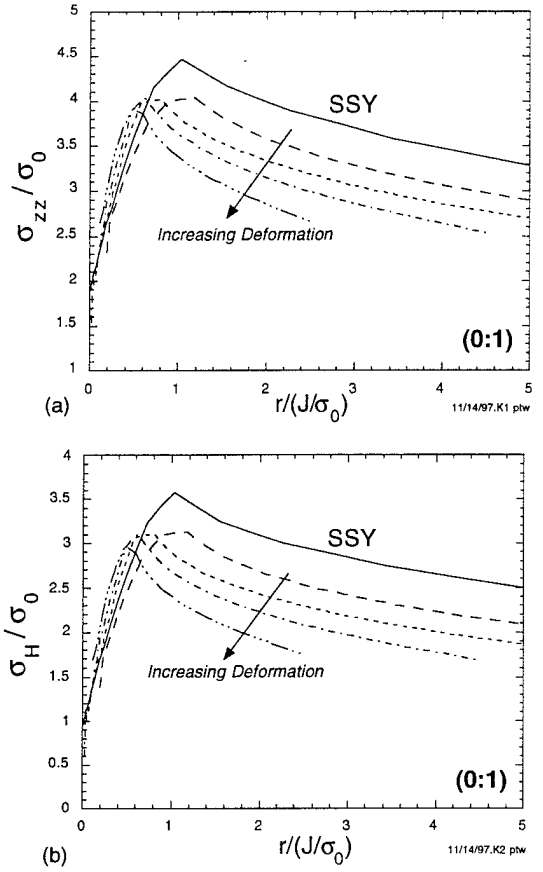

Fig. 13. Comparison of uniaxial (0:1) to SSY solution profiles of (a) opening mode , σ_{zz} , and (b) hydrostatic, σ_H , stresses near the crack tip for J = (66.5, 146.8, 271.7, 469.8 kJ/m^2).

The area enclosed within the specified contour $\sigma_3/\sigma_0 = C$ depends on J and the triaxiality level as quantified by Q. Let A_0 and J_0 represent the area and J-value for the SSY condition with zero T-stress and $Q = 0$ field. If A_f and J_f represent corresponding values in a finite cracked structure having a $Q < 0$ field, then the ratio of J_f / J_0 for which $A_0(\sigma_3/\sigma_0) = A_f(\sigma_3/\sigma_0)$ serves to quantify the size and geometry dependence of fracture toughness. For the latter conditions, a ratio $J_f / J_0 > 1$ implies a loss of constraint in the finite structure that is associated with an increase in measured cleavage fracture toughness.

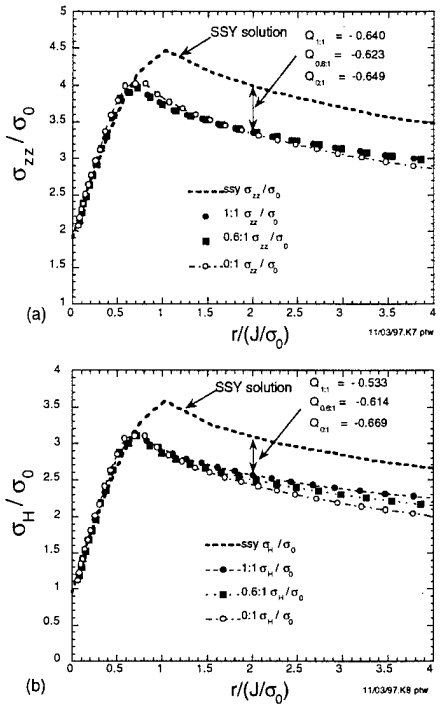

Fig. 14. Sensitivity to biaxiality for Q-stress based on (a) opening mode , σ_{zz} , and (b) hydrostatic, σ_H , stress at $J \approx 131$ kJ/m^2 (0.75 in.-kip/in^2).

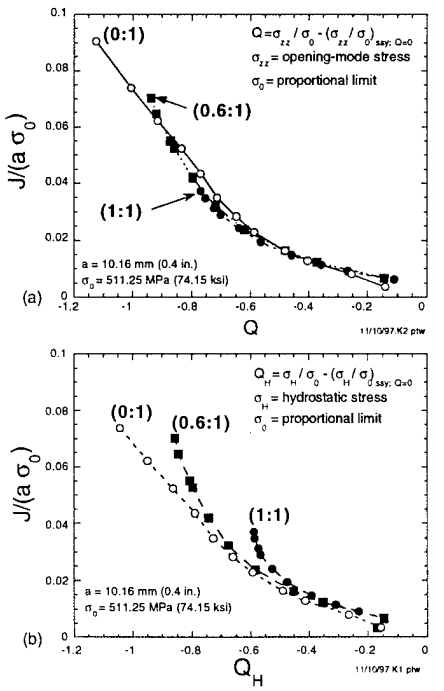

Fig. 15. Evolution of Q-stress at r/(J/σ_0) = 2 based on (a) opening mode , σ_{zz} , and (b) hydrostatic, σ_H , stress.

Computational studies of shallow-flawed, uniaxially-loaded, bend specimens performed by D-A [17] revealed that computed ratios of J_f / J_o are relatively insensitive to the magnitude of the selected σ_3 / σ_0 contour (for sufficiently large values) up to large-scale yielding. The principal stress contours were shown to exhibit a self-similarity that is implied by the *J-Q* relation of Eq. (7); i.e., the shape of the contour is preserved with increasing load as measured by *J*, even though the enclosed area of the contour varies with the hydrostatic stress $Q\sigma_0$. At high loads, this similitude breaks down and the ratio J_f / J_o becomes strongly dependent on the magnitude of σ_3 / σ_0.

Previously, McAfee et al. [5] demonstrated that the D-A toughness scaling model predicted essentially no effect of biaxial loading on cleavage fracture toughness in the cruciform bend specimen due to the insensitivity of in-plane maximum principal stresses to far-field out-of-plane biaxial loading. Recently, analyses were carried out which utilized the hydrostatic stress variable as the failure criterion in the D-A scaling model in place of the maximum principal stress. Applications of this modified D-A model involved integrating over the volume contained within a range of selected hydrostatic stress contours immediately ahead of the crack front for a range of applied loads as measured by *J*. Effective cross-sectional areas for these contours could then be calculated by simply dividing the computed volume by the half-length of the crack front in the finite-element model [x_{max} = 56 mm (2.2 in.)].

Figure 16 shows the variation of the predicted fracture toughness ratio $J_{0:1} / J_{ssy}$ with σ_H / σ_0 for the shallow-flaw cruciform specimen subjected to uniaxial (0:1) loading. Each curve represents a given applied *J*-value, normalized using the constants *a* and σ_0. The ratio $J_{0:1} / J_{ssy}$ is relatively insensitive to the selected σ_H / σ_0 over the interval $1.8 < \sigma_H / \sigma_0 < 2.35$ for the range of applied loads considered in the analysis. In Fig. 17 values of $J_{0:1}$ and J_{ssy}, producing equal-stressed areas of material in the uniaxially loaded cruciform specimen and in the SSY model, are plotted on separate axes. The analysis is based on hydrostatic stress contours having a normalized stress ratio of $\sigma_H / \sigma_o = 2.35$. With increasing load, extensive plastic flow develops in the cruciform specimen and more applied *J* is required to produce the same stressed effective area as compared to the SSY model.

Figure 18 depicts results from a fracture toughness scaling analysis of the cruciform specimen for the three loading cases represented by the measured data in Fig. 9. A value of $\sigma_H / \sigma_0 = 2.35$ was selected as the stress contour for use in the scaling model. In Fig. 18a, the evolution of applied loading (*J*) versus effective area within the contour $\sigma_H / \sigma_0 = 2.35$ is shown for uniaxial and biaxial loading conditions. The *J*-value required to achieve a critical effective area within the critical stress contour decreases with increasing biaxiality ratio. Furthermore, the uniaxial (0:1) loading condition approaches saturation beyond $J = 500$ kJ/m^2; i.e., the area within the critical stress contour no longer increases with increasing applied *J*-value. In contrast, the biaxial loading conditions do not exhibit any tendency to saturate

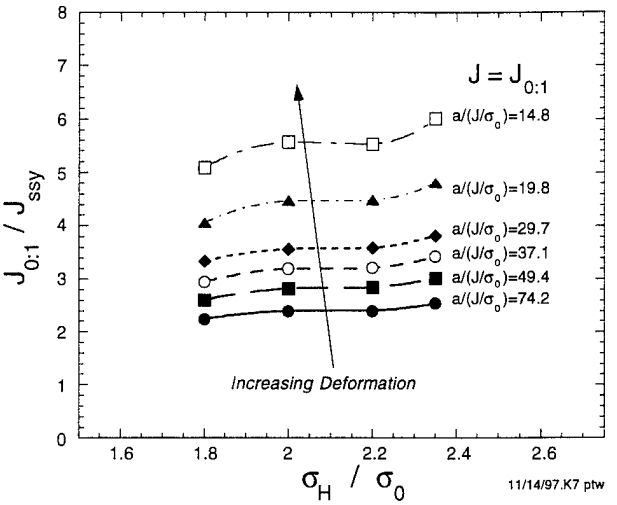

Fig. 16. Ratios of $J_{0:1} / J_{ssy}$ for equivalent areas contained within σ_H / σ_0 contours.

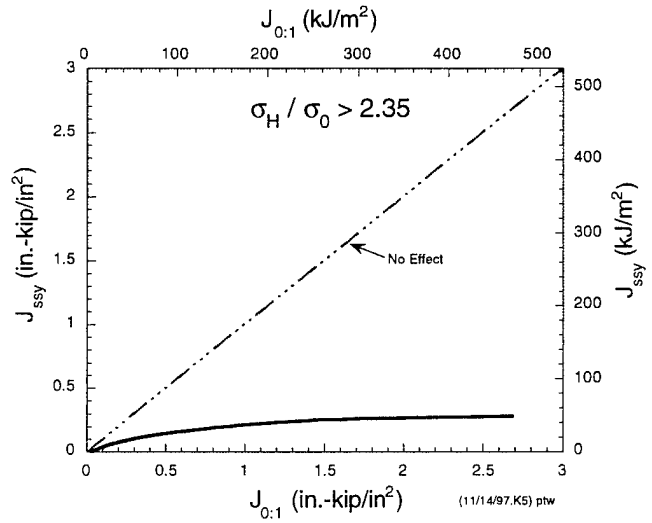

Fig. 17. Areas with equivalent hydrostatic stress: J_{ssy} v. $J_{0:1}$ for $\sigma_H / \sigma_0 > 2.35$.

for the range of loadings considered in the analysis. Analysis results from Fig 18a were used to produce the plots of $J_{x:1}$ v. $J_{0:1}$ (x = 0.6 and 1.0) in Fig. 18b that correspond to equivalent areas of hydrostatic stress within the contour $\sigma_H / \sigma_0 = 2.35$ for the three loading cases. The biaxial loading values were used in place of the conventional SSY values in Fig. 18b in order to compare the relative effects of biaxial and uniaxial loading on the crack tip fields. As demonstrated in Fig. 18b, the departure from the *no-effect* line is significant for both biaxial (0.6:1) and (1:1) loading cases, the effect being more pronounced with increasing biaxiality ratio. Also shown in Fig. 18b are the measured cruciform data for the heat-treated Plate 14 material tested at - 5 °C (Fig. 9), where biaxial data are plotted near the vertical axis and uniaxial data near the horizontal axis. The D-A toughness scaling model, modified to use hydrostatic

stress, is shown to provide an approximate correlation of the effects of biaxial loading on cleavage fracture toughness depicted in Fig. 9, based on a critical contour $\sigma_H / \sigma_0 = 2.35$. Figure 18c presents a $J_{1:1}$ v. $J_{0:1}$ curve for the cruciform specimen based on the maximum principal stress fracture criterion (critical contour $\sigma_3 / \sigma_0 = 2.8$). These results (Fig. 18c) incorrectly predict essentially no effect of biaxial loading on toughness at -5 °C.

Figure 19 illustrates the evolution of the hydrostatic stress contour ahead of the crack tip corresponding to $\sigma_H / \sigma_0 = 2.35$ for both uniaxial (0:1) and biaxial (1:1) loading conditions. For comparable J-values, the area enclosed within the critical stress contour is shown to be greater for the biaxial loading case as compared to the uniaxial case, with the difference becoming more pronounced with increasing J-values.

The sensitivity of $J_{x:1}$ v. $J_{0:1}$ ($x = 0.6$ and 1.0) curves to selection of the critical stress ratio σ_H / σ_0 is depicted in Fig. 20. The curves for both biaxial loading conditions exhibit a significant dependence on stress ratio over the range $1.8 \le \sigma_H / \sigma_0 \le 2.35$. In Fig. 21, this effect is further illustrated in the curves of $J_{0:1} / J_{x:1}$ ratio ($x = 0.6$ and 1.0) for equivalent-stressed areas versus critical σ_H / σ_0 ratio, computed over a range of applied J-values. The dependence is shown to be more pronounced for $\sigma_H / \sigma_0 \le 2.2$. A critical stress ratio of $\sigma_H / \sigma_0 = 2.35$ was selected for the toughness scaling analysis presented in Fig. 18b to provide a reasonable correlation for the measured cruciform data given in Fig. 9.

6.4 Weibull Stress Application

The Weibull methodology implemented in the WSTRESS computer code [22] was used to initiate a study of biaxial loading effects on Weibull stress calculations. The WSTRESS code employs a multiaxial form of the *weakest link* model applicable for a 3-D cracked solid; the Weibull stress, σ_w, is characterized as a fracture parameter reflecting the local damage of the material near the crack tip. The Weibull stress, σ_w, given by the expression

$$\sigma_w = \left[\frac{1}{4\pi V_0} \int_{\Omega} \int_{0}^{2\pi} \int_{0}^{\pi} \sigma_q^m \sin\phi \, d\phi \, d\theta \, d\Omega \right]^{\frac{1}{m}}, \qquad (8)$$

is evaluated by integration of the equivalent stress, σ_q, over the process zone. In Eq. (8), V_0 is the reference volume; m is the Weibull modulus; θ and ϕ are curvilinear coordinates for integration of the tensile stress; and Ω denotes the volume of the near-tip fracture process zone. A fracture criterion must be specified to determine the equivalent (tensile) stress, σ_q, acting on a microcrack included into the fracture process zone. In this study, the equivalent stress was taken to be (1) the maximum principal stress, σ_3, and (2) the hydrostatic stress, σ_H, acting on all material points in the element. For these two choices of equivalent stress, the values of σ_q are independent of microcrack location and orientation, and the Weibull stress is, therefore,

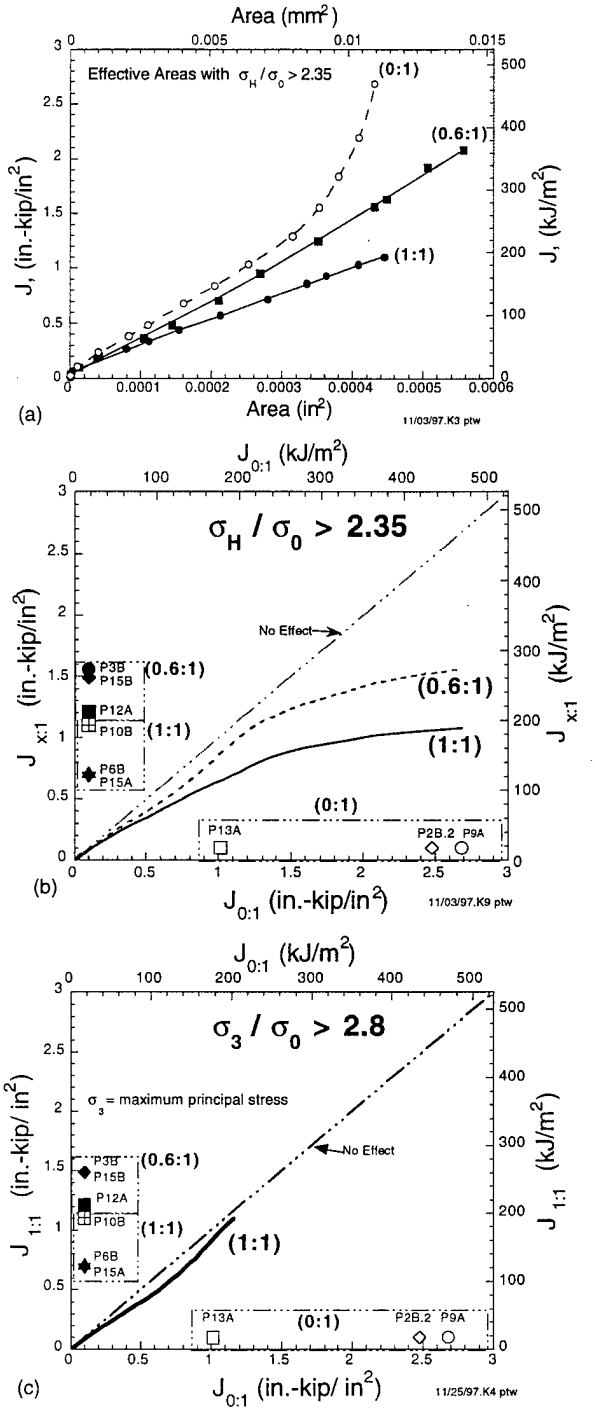

Fig. 18. Areas of equivalent stress with initiation loads for uniaxial and biaxial cruciform test specimens: (a) J v. effective area for $\sigma_H / \sigma_0 \ge 2.35$, (b) $J_{x:1}$ v. $J_{0:1}$ for $\sigma_H / \sigma_0 \ge 2.35$, and (c) $J_{1:1}$ v. $J_{0:1}$ for $\sigma_3 / \sigma_0 \ge 2.8$.

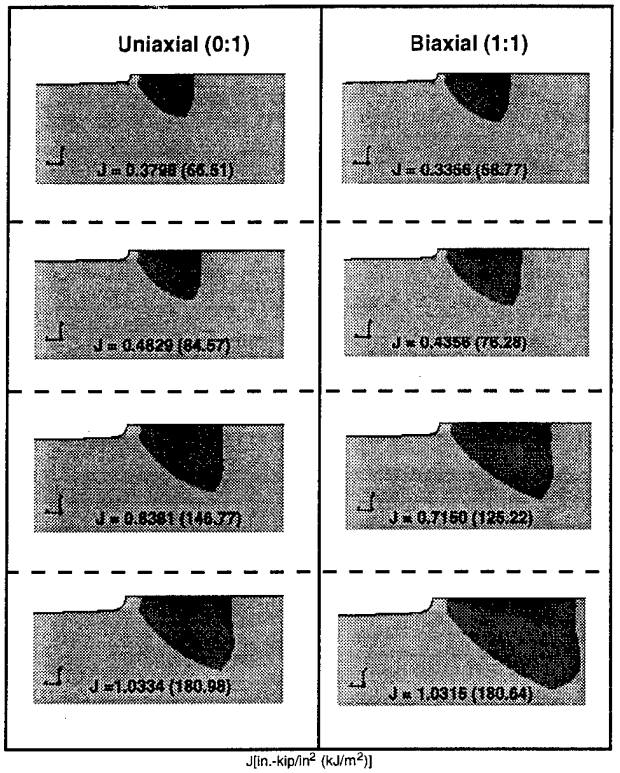

Fig. 19. Contours of hydrostatic stress near the crack tip: $\sigma_H / \sigma_0 = 2.35$.

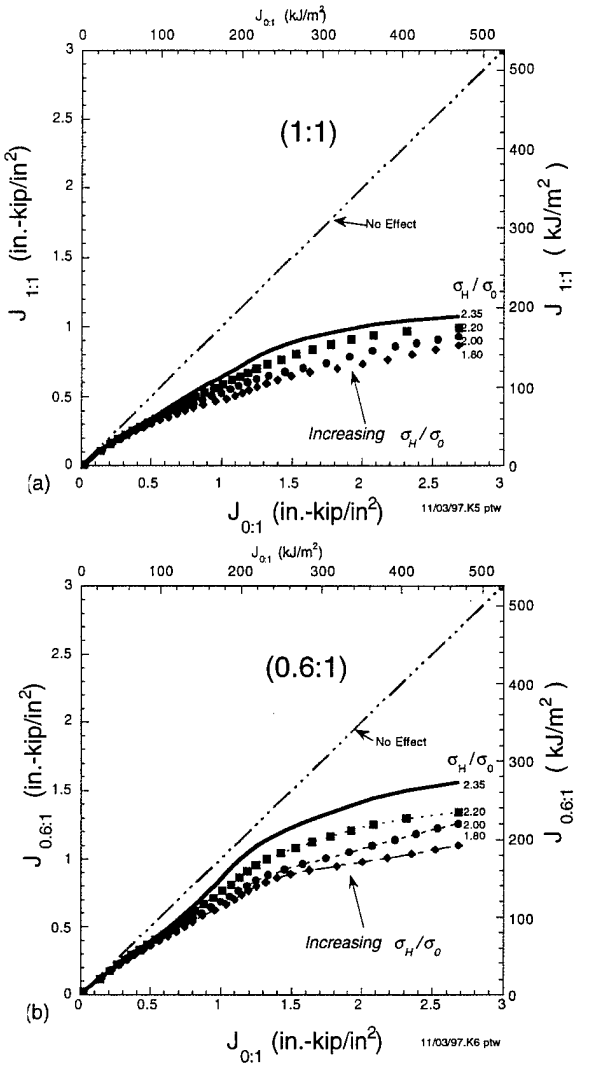

Fig. 20. Sensitivity of $J_{x:1}$ v. $J_{0:1}$ to selection of critical σ_H / σ_0 for (a) (1:1) and (b) (0.6:1) loading cases

$$\sigma_w = \left[\frac{1}{V_0} \int_{\Omega} \sigma_q^m \, d\Omega \right]^{\frac{1}{m}} , \qquad (9)$$

where $\sigma_q = \sigma_3$ or σ_H.

Figure 22 compares calculations of the Weibull stress in the cruciform specimen subjected to uniaxial (0:1) and biaxial (1:1) loading conditions for a range of J-values. In Fig. 22a, the equivalent stress was set to the maximum principal stress, and the Weibull stress was then calculated for values of the modulus m = 8, 10, and 20. No significant effects of biaxial loading were detected for the three m values using the maximum principal stress criterion. In Fig. 22b, the calculation is repeated with the equivalent stress taken as the hydrostatic stress. Differentiation between uniaxial (0:1) and biaxial (1:1) loading can be observed when the Weibull modulus m is set to values of 8 and 10. By increasing the Weibull modulus to 20, any distinction between uniaxial and biaxial loading is essentially lost.

For m fixed at some value in Fig. 22b (i.e., m = 8 or 10), a (constant) critical Weibull stress is determined by locating a fracture toughness data point from a uniaxial test on the uniaxial Weibull stress curve. A predicted (lower) fracture toughness corresponding to fully biaxial loading is established from intersection of that line of critical Weibull stress with the biaxial Weibull stress curve. Further studies are under way to develop the proper methodology for characterizing a Weibull model that can reflect the biaxial loading effects on fracture toughness observed in the data of Fig. 9.

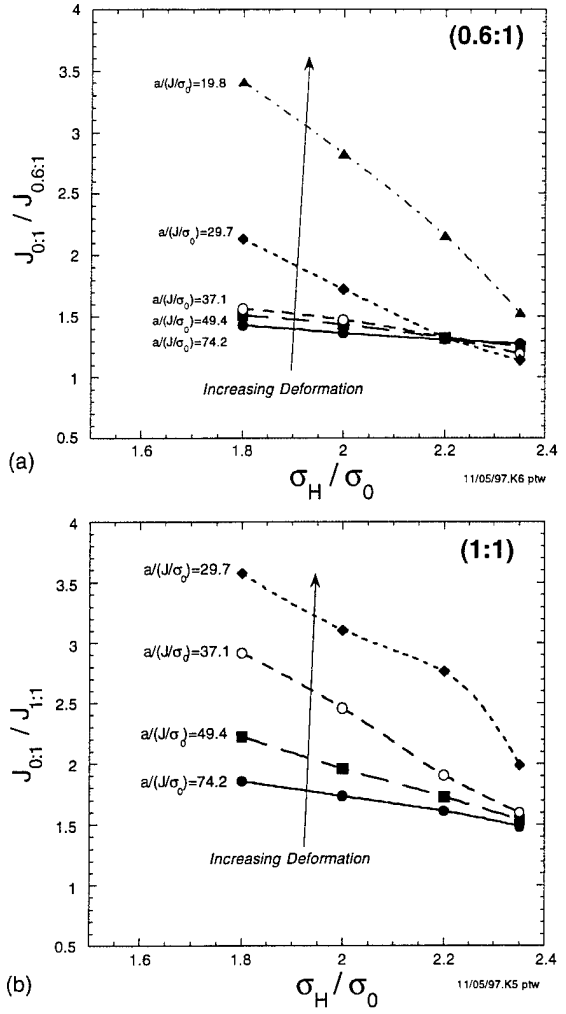

Fig. 21. Sensitivity of $J_{0:1} / J_{x:1}$ ratios with equivalent areas to selection of critical σ_H / σ_0 for (a) (0.6:1) and (b) (1:1) loading cases.

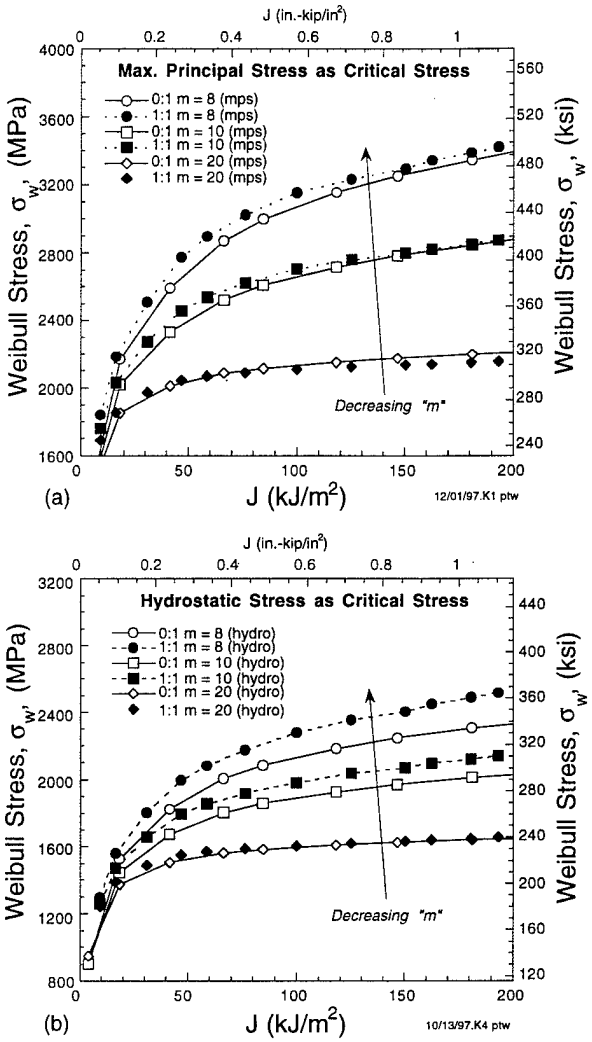

Fig. 22. Weibull stresses with (a) maximum principal stress, σ_3 , and (b) hydrostatic stress, σ_H , as the equivalent stress, σ_q .

7. Results and Conclusions

A technology is being developed to determine shallow-flaw fracture toughness of RPV steels under prototypic biaxial loading conditions for application to the safety assessment of RPVs. Tests of cruciform bend specimens demonstrated that biaxial loading can have a pronounced effect on shallow-flaw fracture toughness in the lower transition temperature region for RPV materials.

For temperatures near the lower shelf, essentially no biaxial effect was observed. At a test temperature only 25 °C higher, full equibiaxial (1:1) loading reduced toughness to approximately 58 percent of the average toughness obtained from uniaxial tests. For the small number of data points described herein, scatter in the estimated toughness values under biaxial loading was significantly reduced as compared to the scatter normally observed in conventional compact tension or single edge notch beam specimens tested in the transition temperature region. Under conditions where a biaxial effect was observed, biaxial loading also affected the deformation at failure as measured by both CMOD and LLD. Increasing the biaxiality ratio correlated with reducing the deformation at failure. Additional tests are planned at -5 °C to better quantify the mean fracture toughness and scatter for biaxial (1:1) loading.

The cruciform fracture toughness data are being used to evaluate fracture methodologies for predicting the observed effects of biaxial loading on shallow-flaw fracture toughness. Initial emphasis was placed on assessment of stress-based methodologies, namely, the *J-Q* formulation, the D-A toughness scaling model, and the Weibull approach. Applications of these methodologies based on the hydrostatic stress fracture criterion indicated an effect of biaxiality on fracture toughness; the maximum principal stress criterion,

however, indicated no effect of biaxiality at -5 °C, contrary to the experimental test results.

Specifically, our conclusions are:

- The Q_H-stress parameter, based on hydrostatic stress, implies that a higher level of crack-tip constraint is maintained under increasing load as the biaxiality ratio is varied from uniaxial (0:1) to equibiaxial (1:1) conditions.
- The D-A toughness scaling model was shown to provide an approximate correlation of the effects of biaxial loading on cleavage fracture toughness for a limited data set, based on a critical contour $\sigma_H / \sigma_0 = 2.35$. The curves of $J_{0:1} / J_{x:1}$ ratio ($x = 0.6$ and 1.0) for equivalent-stressed areas versus critical σ_H / σ_0 ratio exhibited a significant dependence on stress ratio over the range $1.8 \leq \sigma_H / \sigma_0 \leq 2.35$.
- With the hydrostatic stress as the equivalent stress, differentiation between uniaxial (0:1) and biaxial (1:1) loading was observed when the Weibull modulus m is set to values of 8 and 10 in the Weibull stress integral; however, this differentiation disappears for m equal to 20.
- Experimental and analytical results presented herein provide the motivation to reconsider micromechanical models of cleavage fracture initiation and to develop a metallurgically-based argument for σ_H as a driver of cleavage fracture under multiaxial loading conditions.

Acknowledgment

The authors wish to thank Professor Robert H. Dodds, Jr., University of Illinois, for his many helpful contributions to the constraint applications described in this paper.

References

1. T. H. Theiss and D. K. M. Shum, *Experimental and Analytical Investigation of the Shallow-Flaw Effect in Reactor Pressure Vessels,* USNRC Report NUREG/CR-5886 (ORNL/TM-12115), Oak Ridge National Laboratory, July 1992.
2. B. R. Bass, J. A. Keeney, and W. J. McAfee, "Assessment of the Fracture Behavior of Weld Material from a Full-Thickness Clad RPV Shell Segment," *Fatigue and Fracture Mechanics in Pressure Vessels and Piping, ASME Pressure Vessel and Piping Conference*, Honolulu, Hawaii, July 23-27, 1995, PVP-Vol. 304, pp. 299-311.
3. W. J. McAfee, B. R. Bass, and J. W. Bryson, Jr., "Development of a Methodology for the Assessment of Shallow-Flaw Fracture in Nuclear Reactor Pressure Vessels," *ASME Pressure Vessel and Piping Conference*, Orlando, Florida, July 27-31, 1997, PVP-Vol. 346, pp. 85-94.
4. W. E. Pennell, B. R. Bass, J. W. Bryson, Jr., T. L. Dickson, and J. G. Merkle, "Preliminary Assessment of the Effects of Biaxial Loading on Reactor Pressure Vessel Structural-Integrity-Assessment Technology," *Proceedings of 4th ASME/JSME International Conference in Nuclear Engineering*, New Orleans, Louisiana, March 10-14, 1996.
5. W. J. McAfee, B. R. Bass, J. W. Bryson, Jr., and W. E. Pennell, *Biaxial Loading Effects on Fracture Toughness of Reactor Pressure Vessel Steel,* USNRC Report NUREG/CR-6273 (ORNL/TM-12866), Oak Ridge National Laboratory, March 1995.
6. T. H. Theiss et al., *Initial Results of the Influence of Biaxial Loading on Fracture Toughness,* USNRC Report NUREG/CR-6132 (ORNL/TM-12498), Oak Ridge National Laboratory, July 1994.
7. B. R. Bass, W. J. McAfee, J. W. Bryson, Jr., and W. E. Pennell, "Determination of Cladding Effects on Shallow-Flaw Fracture Toughness of Reactor Pressure Vessel Steel under Prototypic Biaxial Loading," *5th International Conference on Nuclear Engineering*, Nice, France, May 26-30, 1997.
8. S. G. Larsson and A. J. Carlson, "Influence of Non-Singular Stress Terms and Specimen Geometry on Small Scale Yielding at Crack-Tips in Elastic-Plastic Materials," *Journal of the Mechanics and Physics of Solids* **21**, 447-473 (1973).
9. N. P. O'Dowd and C. F. Shih, "Family of Crack-Tip Fields Characterized by a Triaxiality Parameter: Part I - Structure of Fields," *Journal of the Mechanics and Physics of Solids* **39**(8), 989-1015 (1991).
10. R. H. Dodds, Jr., T. L. Anderson, and M. T. Kirk, "A Framework to Correlate a/W Ratio Effects on Elastic-Plastic Fracture Toughness (J_c)," *Int. J. Frac.* **48**, 1-22 (1991).
11. T. L. Anderson and R. H. Dodds, Jr., "Specimen Size Requirements for Fracture Toughness Testing in the Ductile-Brittle Transition Region," *J. Test. Eval.* **19**, 123-134 (1991).
12. C. Ruggieri and R. H. Dodds, Jr., "Probabilistic Modeling of Brittle Fracture Including 3-D Effects on Constraint Loss and Ductile Tearing," in *International Conference on Local Approach to Fracture (MECAMAT 96),* Fontainebleau, France, 1996.
13. A. G. Evans, "A General Approach for the Statistical Analysis of Multiaxial Fracture," *J. Am. Ceram. Soc.,* **61** (7-8), 302-308 (1978).
14. S. B. Batdorf and H. L. Heinisch, Jr., "Weakest-Link Theory Reformulated for Arbitrary Fracture Criterion," *J. Am. Ceram. Soc.,* **61** (7-8), 355-358 (1978).
15. T. Thiemeier and A. Brückner-Foit, "Influence of the Fracture Criterion on the Failure Prediction of Ceramics Loaded in Biaxial Flexure," *J. Am. Ceram. Soc.,* **74** (1), 48-52 (1991).
16. V. Weiss, "Material Ductility and Fracture Toughness of Metals," *Proceedings of the International Conference on Mechanical Behavior of Materials*, Kyoto, Japan, August 15-20, 1971, The Society of Materials Science, Japan, 1972.
17. R. H. Dodds, Jr., C. F. Shih, and T. L. Anderson, *Continuum and Micromechanics Treatment of Constraint in Fracture,* UILU-ENG-92-2014, Dept. of Civil Engineering, University of Illinois, Urbana, Illinois, November 1992.
18. R. K. Nanstad et al., *Irradiation Effects on Fracture Toughness of Two High-Copper Submerged-Arc Welds, HSSI Series 5,* USNRC Report NUREG/CR-5913 (ORNL/TM-12156/V1), Oak Ridge National Laboratory, October 1992.

19. D. E. McCabe, U. Zerbst, and J. Heerens, *Development of Test Practice Requirements for a Standard Method of Fracture Toughness Testing in the Transition Range*, GKSS Report 93/E/81, GKSS Forschungszentrum, Geesthacht, GmBH, Germany, 1993.
20. *ABAQUS Theory Manual*, Version 5.5, (Hibbitt, Karlson, and Sorenson, Inc., Providence, Rhode Island, 1996).
21. J. G. Merkle, *An Examination of the Size Effects and Data Scatter Observed in Small-Specimen Cleavage Fracture Toughness Testing*, USNRC Report NUREG/CR-3672 (ORNL/TM-9088), Oak Ridge National Laboratory, April 1984.
22. C. Ruggieri and R. H. Dodds, Jr., *WSTRESS: Numerical Computation of Probabilistic Fracture Parameters,* UILU-ENG-95-2013, Department of Civil Engineering, University of Illinois, Urbana, Illinois, September 1996 (Revised).

Report Number (14) ORNL/CP--96312
CONF-980708--

Publ. Date (11) 19980[illegible]
Sponsor Code (18) NRC, XF
UC Category (19) UC-000, DOE/ER

DOE